Real-time photoacoustic imaging system for burn diagnosis

Taiichiro Ida
Yasushi Kawaguchi
Satoko Kawauchi
Keiichi Iwaya
Hitoshi Tsuda
Daizoh Saitoh
Shunichi Sato
Toshiaki Iwai

Real-time photoacoustic imaging system for burn diagnosis

Taiichiro Ida,[a,*] **Yasushi Kawaguchi,**[a] **Satoko Kawauchi,**[b] **Keiichi Iwaya,**[c] **Hitoshi Tsuda,**[c] **Daizoh Saitoh,**[d] **Shunichi Sato,**[b] **and Toshiaki Iwai**[e]

[a]New Concept Product Initiative, Advantest Corporation, 1-5, Shin-tone, Kazo-shi, Saitama 349-1158, Japan
[b]National Defense Medical College Research Institute, Division of Biomedical Information Sciences, 3-2, Namiki, Tokorozawa-shi, Saitama 359-8513, Japan
[c]National Defense Medical College Research Institute, Department of Basic Pathology, 3-2, Namiki, Tokorozawa-shi, Saitama 359-8513, Japan
[d]National Defense Medical College Research Institute, Division of Basic Traumatology, 3-2, Namiki, Tokorozawa-shi, Saitama 359-8513, Japan
[e]Tokyo University of Agriculture and Technology, Graduate School of Bio-Applications and Systems Engineering, 2-24-6, Naka-cho, Koganei-shi, Tokyo 184-8588, Japan

Abstract. We have developed a real-time (8 to 30 fps) photoacoustic (PA) imaging system with a linear-array transducer for burn depth assessment. In this system, PA signals originating from blood in the noninjured tissue layer located under the injured tissue layer are detected and imaged. A compact home-made high-repetition-rate (500 Hz) 532-nm fiber laser was incorporated as a light source. We used an alternating arrangement for the fibers and sensor elements in the probe, which improved the signal-to-noise ratio, reducing the required laser energy power for PA excitation. This arrangement also enabled a hand-held light-weight probe design. A phantom study showed that thin light absorbers embedded in the tissue-mimicking scattering medium at depths >3 mm can be imaged with high contrast. The maximum error for depth measurement was 140 μm. Diagnostic experiments were performed for rat burn models, including superficial dermal burn, deep dermal burn, and deep burn models. Injury depths (zones of stasis) indicated by PA imaging were compared with those estimated by histological analysis, showing discrepancies <200 μm. The system was also used to monitor the healing process of a deep dermal burn. The results demonstrate the potential usefulness of the present system for clinical burn diagnosis. © *The Authors. Published by SPIE under a Creative Commons Attribution 3.0 Unported License. Distribution or reproduction of this work in whole or in part requires full attribution of the original publication, including its DOI.* [DOI: 10.1117/1 .JBO.19.8.086013]

1 Introduction

For severe burn patients, the depth and area of injury are two crucial factors determining long-term function and mortality. In terms of injury depth, burns are classified into epidermal burn, superficial dermal burn (SDB), deep dermal burn (DDB), and deep burn (DB). The treatment plan and strategy differ depending on the injury depth. In cases of DDB, in which injury reaches the deep dermis, the injury is often exacerbated by infection, and antibiotic treatment is important. In cases of DB (full thickness burn), spontaneous tissue regeneration does not occur and skin grafting is required. Thus, differentiation between SDB and DDB and differentiation between DDB and DB are crucially important in a clinical situation. Currently, however, diagnosis of burn depths mainly relies on visual observation, which is often difficult and inaccurate. Thus, many efforts have been made to develop a valid system for clinical burn diagnosis. Various systems, including a laser Doppler blood flow imager,[1] polarization-sensitive optical coherence tomography,[2] and a video microscope,[3] have been developed and tested, but their measurement depths are limited to ~1 mm or less, which is not sufficient for human skin diagnosis, or the measurement is not quantitative in principle.

Photoacoustic (PA) burn diagnosis was first reported by Sato et al.[4] In this method, PA signals originating from blood in the noninjured tissue layer, which is located under the injured tissue layer with blood occlusion (zone of stasis), are detected. Since hyperemia occurs just under the zone of stasis, we can obtain high-contrast PA signals indicating the depth of injury. Experiments using rat burn models showed the validity of this method. In those experiments, however, the measurement depth was limited to ~2 mm and a single-element transducer was used, with which real-time imaging was not possible. In this study, we developed a real-time PA imaging system with a measurement depth >3 mm as a prototype for clinical burn diagnosis.

We intended to make a movable whole-in-one type system with a handheld probe that resembles conventional ultrasound imaging probes for ease of handling by clinicians. Various types of PA imaging systems have been developed and examined for burn depth assessment, including an acoustic-resolution PA microscopy system[5] and a system based on a 128-element linear sensor array.[6] To the authors' knowledge, however, a movable whole-in-one PA burn diagnostic system with a handheld probe has not yet been reported. In this paper, the design and structure of the system and the results of experiments using originally made skin tissue phantoms and rat burn models are described. The system was also used to monitor the healing process of a burn in a rat, providing some new insights.

*Address all correspondence to: Taiichiro Ida, E-mail: taiichiro.ida@jp .advantest.com

2 Materials and Methods

2.1 System Specifications

A block signal diagram of the PA imaging system for burn depth assessment is shown in Fig. 1(a). The repetition rate and size of the light source for PA excitation determine imaging speed and total size of the system, respectively. We decided to incorporate an originally developed high-repetition-rate (500 Hz) 532-nm fiber laser (pulse width, 20 ns)[7] into the system. For the probe design, we examined various configurations of optical fibers and sensor elements to maximize the PA signal-to-noise ratio and to reduce the size and weight for handheld use. For a linear array sensor, optical fibers for PA excitation are often placed on one side or both sides of the sensor array, but we chose an alternating arrangement for fibers and sensor elements as shown in Fig. 1(b); eight Pb(Zr,Ti)O^3 elements (center frequency, 10 MHz) and nine optical fibers are alternately arranged for a measurement length of $\sim$10 mm. With this configuration, the PA signal-to-noise ratio was considerably improved due to the spatial matching of the sensing zone and photon distribution in tissue. This design also enabled reduction of the required total laser energy as well as the size (40 mm^L $\times$ 20 to 30 mm^W $\times$ 170 mm^H) and weight (170 g) of the probe [Fig. 1(c)]. In addition, a compact fiber laser (350 mm^L $\times$ 400 mm^W $\times$ 60 mm^H) was adapted to the system. The laser output is coupled to a fiber bundle and divided into nine optical fibers as described above. The total delivered laser pulse energy is 300 μJ and the light intensity at the imaging head bottom surface, which is placed on the skin, is 140 mW/cm^2. This is lower than the ANSI safety limit of 200 mW/cm^2. Detected PA signals are digitized at 250 megasamples per second on a custom-designed board and sent to a large-scale field-programmable gate array, which performs digital signal processing and a phased-array process. The data are sent to a PC through a USB interface, enabling real-time two-dimensional (2-D) PA imaging with a maximum frame rate of 30 fps. All of the PA images described in this paper were constructed by using a constant sound velocity of 1530 m/s. A photograph of the whole-in-one system is shown in Fig. 1(d).

2.2 Phantom Study

To evaluate imaging characteristics of the present system, phantoms mimicking skin tissue were made. To imitate the layered structure of the skin, the phantoms are sheet-type and stackable. The method of fabrication and characteristics of the phantoms are described in Ref. 8. Briefly, the host material was an acrylic block soft copolymer, in which titanium oxide nanoparticles were mixed as light scatterers. Water-soluble red ink (BCI-326M, Canon, Tokyo, Japan) was used as a light absorber. To mimic the vasculature, a line mesh pattern with the ink was printed on the polymer sheet by an ink-jet printer (see schematics on the left of Fig. 2). Optical properties of the phantoms were measured by the standard method using an integrated sphere and a spectrometer, and the scattering and absorption coefficients were adjusted to be 2.4 and 0.022 mm^{-1}, respectively; the relative density was 1.08.[9,10] The thickness of each sheet-type phantom was designed to be 0.7 mm; the fabrication error of each sheet thickness was 30 to 40 μm.

2.3 Burn Depth Assessment

All animal experiments were carried out in accordance with the Guide for Laboratory Animal Facilities and Care Regulation of the National Defense Medical College, Saitama, Japan. To validate the usefulness of the present PA imaging system for burn depth assessment, we performed experiments using rat burn models. With a Walker-Mason template,[11] an SDB, DDB, or DB of $\sim$20% of the total body surface area was induced in the rat dorsal skin. With the system, PA imaging was performed on the wounds at 48 h postburn, and then tissues at the measurement sites were biopsied and sectioned. The sections were then fixed and stained with hematoxylin and eosin (H&E). The PA images were compared with the results of histological analysis. The number of rats that underwent 2-D PA imaging was six for each model including the control.

Three-dimensional (3-D) imaging was also performed for the burn-nonburn interface region in the rat with a DB, for which an imaging head was scanned over the wound and the adjacent skin for a length of 32 mm with a step size of 0.2 mm. One hundred and sixty 2-D images were converted to a 3-D image by using volume visualization software (VolView 3.4, Kitware Inc., Clifton Park, New York).

2.4 Monitoring of the Burn Healing Process

Using the same system as that described above, PA imaging was performed for DDBs in rats at one, three, and five days postburn.
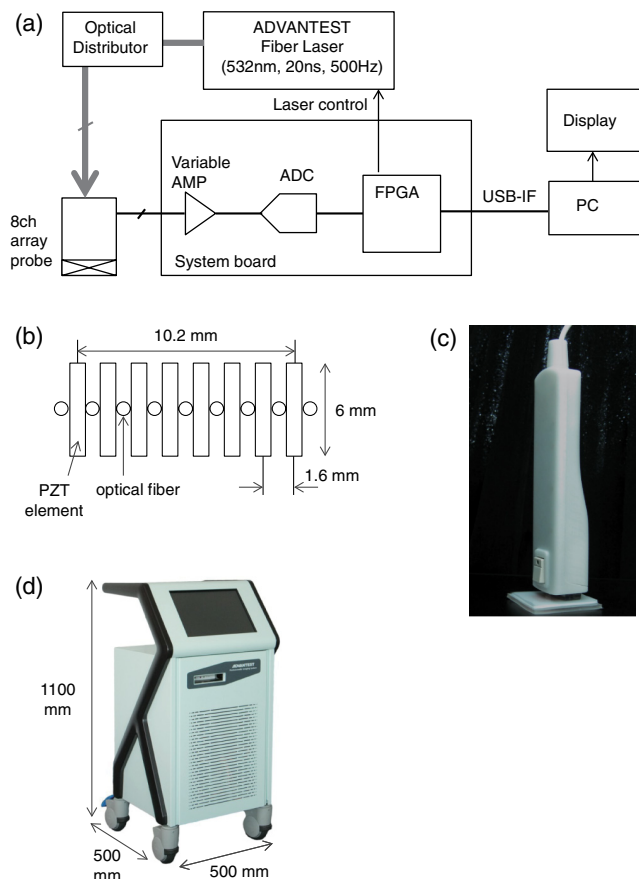

Fig. 1 Photoacoustic (PA) imaging system for burn diagnosis. (a) Block signal diagram. (b) Arrangement of optical fibers and sensor elements in the imaging head (probe). Photographs of the imaging head (c) and the whole system (d).
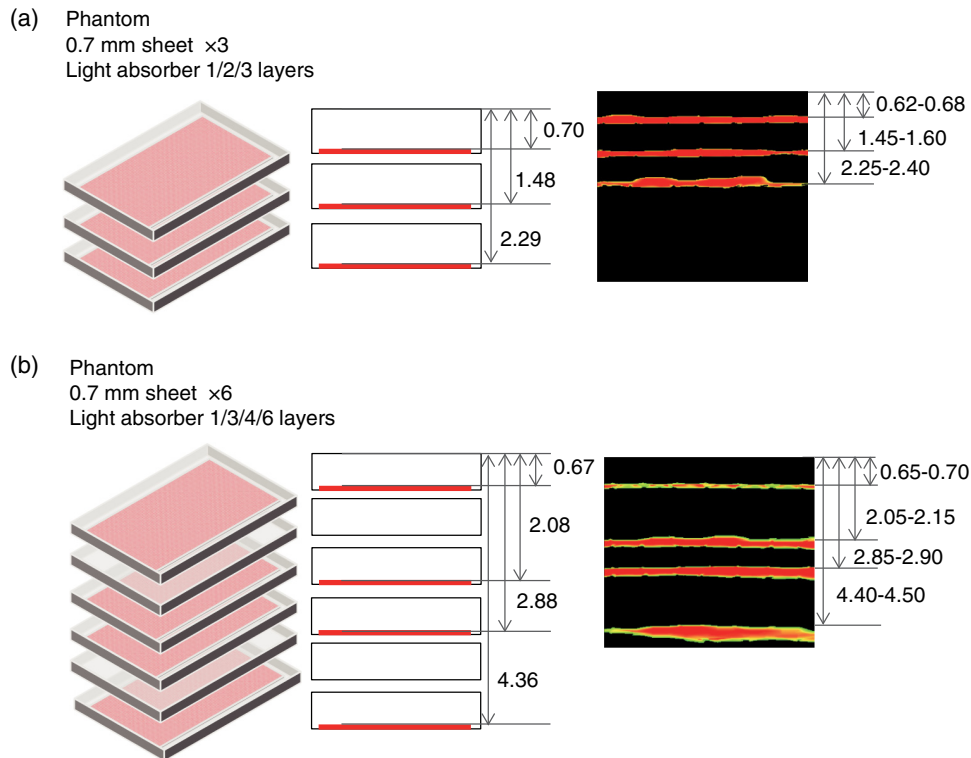
(a) Phantom
0.7 mm sheet ×3
Light absorber 1/2/3 layers

(b) Phantom
0.7 mm sheet ×6
Light absorber 1/3/4/6 layers

Fig. 2 Results of depth measurement of each absorption layer by using digital micrometer calipers and PA imaging for two types of skin-mimicking phantoms: three-layered model (a) and six-layered model, including two layers without an absorption pattern (b). Caliper-measured depths of absorption layers are shown on the right of the schematics of phantoms. Range of depths at which a PA signal arises for each absorption layer is shown on the right of each PA image.

These time points were chosen on the basis of the results of our previous study using a single-element PA sensor, which showed angiogenesis in the wound within five days postburn by histological analysis, while PA signals originating from neovascularities were not clearly detected due to limited resolution.[12] In this study, the tissue was biopsied after each PA imaging and a sample with H&E staining was made. The PA images were compared with the results of histological analysis. The number of rats that underwent PA imaging for monitoring the healing process was four at each time point; two of them underwent biopsy.

3 Results and Discussion

3.1 *Phantom Study*

Figure 2 shows the results of depth measurement of each absorption layer by using digital micrometer calipers (MDQ-30, Mitsutoyo, Kanagawa, Japan) and PA imaging for two types of phantoms: a simple three-layered model and a six-layered model, in which mesh patterns were not printed on the second and fifth layers. For the three-layered model, the depths at which signals arose for the first (depth measured by calipers, 0.70 mm), second (1.48 mm), and third (2.29 mm) absorption layers were 0.62 to 0.68 mm (maximum error for the depth measured by calipers, 80 μm), 1.45 to 1.60 mm (120 μm), and 2.25 to 2.40 (110 μm), respectively. For the six-layered model, the depths at which signals arose for the first (depth measured by calipers, 0.67 mm), second (2.08 mm), third (2.88 mm), and fourth (4.36 mm) absorption layers were 0.65 to

0.70 mm (maximum error for the depth measured by calipers, 30 μm), 2.05 to 2.15 mm (70 μm), 2.85 to 2.90 mm (30 μm), and 4.40 to 4.50 mm (140 μm), respectively. Thus, the maximum imaging depth error for the phantoms was 140 μm, although this value may be affected by the compression with a sensor for soft material and biological tissue. Since the deepest absorption layer at ∼4 mm can be visualized with high contrast, the results show the capability of visualizing vasculatures in full-thickness human skin tissue with the present imaging system.

3.2 *Burn Depth Assessment*

Figure 3 shows histological images and the corresponding PA images of the normal skin [Figs. 3(a1)–3(a3)], SDB [Figs. 3(b1)–3(b3)], DDB [Figs. 3(c1)–3(c3)], and DB [Figs. 3(d1)–3(d3)]. Figures 3(a3)–3(d3) are magnified versions of the regions indicated by white line 1 mm squares in Figs. 3(a2)–3(d2). The thicknesses of the normal skin were ∼1.0 mm or less, but it should be noted that burned skin became thicker due to edema and collagen deterioration; skin thicknesses of the skin with an SDB, DDB, and DB were ∼1.2, ∼1.6, and ∼1.7 mm, respectively.

In the histological image of the normal skin, blood vessels just under the epidermis can be clearly seen [Fig. 3(a3)]. In the shallowest region of the corresponding PA image [Fig. 3(a1)], two different signals, the surface signal due to contamination and/or pigmentation and the signal originating from blood vessels just under the epidermis, are overlapped and the signal layer is, therefore, broadened. In the histological image of the SDB, the epidermis and superficial part of the skin appendages are
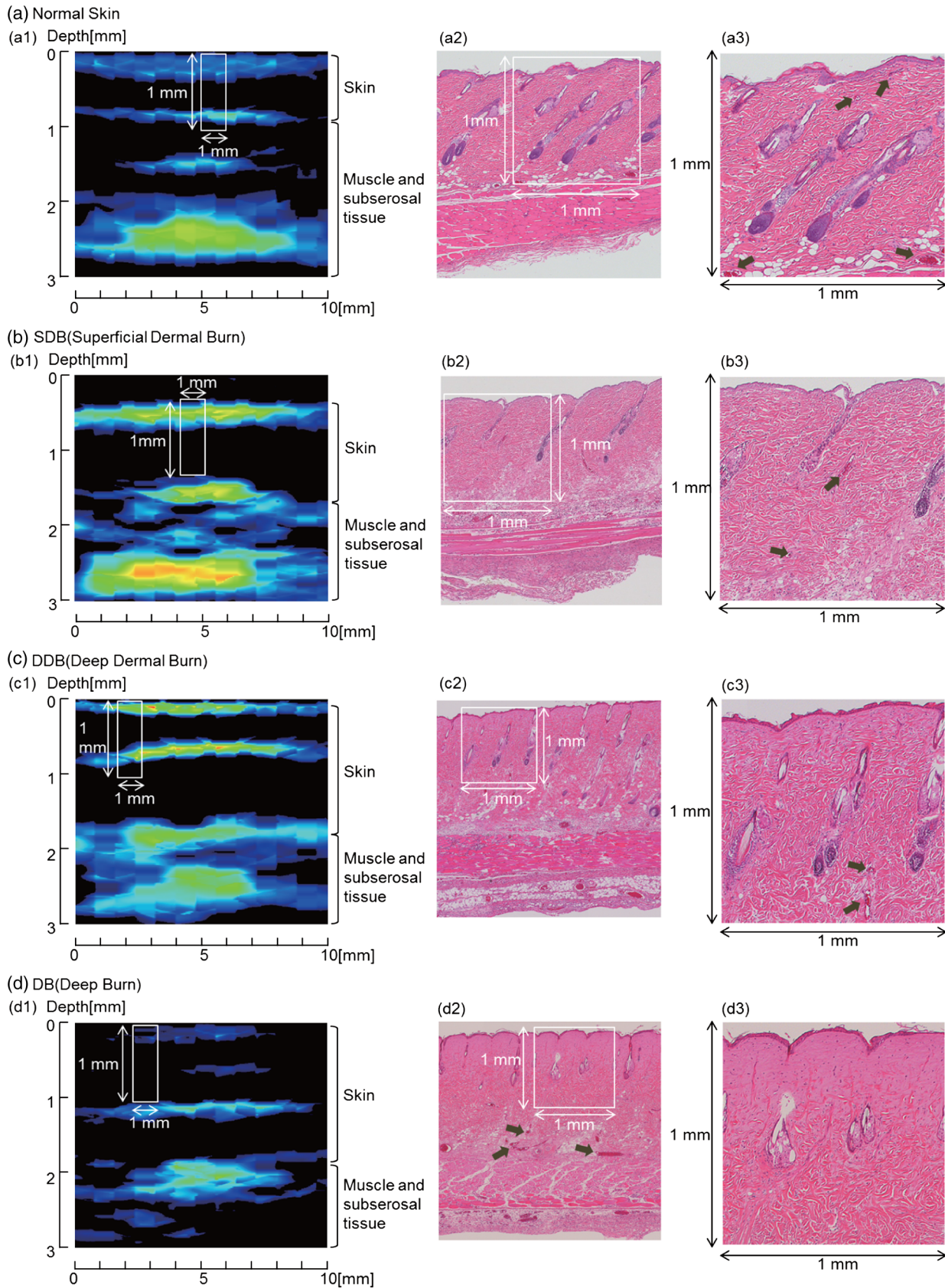
Fig. 3 Histological images with hematoxylin and eosin (H&E) staining and the corresponding PA images of the normal skin [(a1) to (a3)], superficial dermal burn [(b1) to (b3)], deep dermal burn [(c1) to (c3)], and deep burn (DB) [(d1) to (d3)]. (a3) to (d3) are magnified versions of the regions indicated by white line 1 mm squares in (a2) to (d2). White line rectangles in PA images [(a1) to (d1)] correspond to the regions shown in (a3) to (d3). Arrows in (a3), (b3), (c3), and (d2) indicate viable blood vessels.

Table 1 Depths of damaged tissues (zones of stasis) estimated by histological analysis and by photoacoustic (PA) imaging.

	Control (mm)	Superficial dermal burn (mm)	Deep dermal burn (mm)	Deep burn (mm)
Histological analysis				
Skin thickness (depth from epidermis to subcutaneous tissue	~1.0	~1.2	~1.6	~1.7
Depth of damaged tissue	0	0 to 0.2	0.3 to 0.6	0.6 to 0.9
Estimation by PA imaging				
Depth of vascular occlusion	0	0	0.4 to 0.6	0.8 to 1.0

injured, where blood vessels indicated by arrows seem to be viable but with infiltration of a few neutrophils [Figs. 3(b2) and 3(b3)]. In the corresponding PA image [Fig. 3(b1)], the surface signal and the signal originating from blood vessels under the epidermis are also overlapped, but the signal is much stronger, which is attributable to hyperemia. In the histological image of DDB, the epidermis and upper two thirds of the dermis are damaged, where blood vessels are not observed clearly, while blood vessels with erythrocytes remain at depths of ~1 mm [Figs. 3(c2) and 3(c3)]. In the corresponding PA image [Fig. 3(c1)], the shallowest signal layer is thin due to the occlusion of blood vessels just under the epidermis, and a zone of stasis as deep as ~0.8 mm can be clearly seen. In the histological image of DB, collagen fibers in a large part of the dermis are fused and no blood vessels are seen at depths up to ~1.0 mm; there are some dilated blood vessels at depths of ~1.2 mm [Figs. 3(d2) and 3(d3)]. The zone of stasis as deep as ~1.0 mm is shown in the corresponding PA image [Fig. 3(d1)]. The depths of damaged tissues (zones of stasis) estimated by histological analysis and those estimated by PA imaging are summarized in Table 1. Discrepancies between the results of histological analysis and those obtained by PA imaging were in the range of 100 to 200 μm. Due to the artifact in the preparation of tissue samples for histological analysis, it is difficult to evaluate measurement errors in an *in vivo* study. In addition, change in the sound velocity of coagulated tissue may affect the results of PA imaging. Thus, further study is needed to accurately estimate errors in *in vivo* diagnosis of burn depth by the PA imaging. On the basis of the errors shown by the phantom study, however, the present system seems to have a potential to be used for clinical burn diagnosis.

Figure 4 shows results of 3-D PA imaging of the burn (DB)-nonburn interface region. A drastic change in the zone of stasis is shown at the boundary. The first (shallowest) signal layer clearly seen in the nonburn tissue has completely disappeared in the burned tissue, indicating the formation of a zone of stasis as also shown by the 2-D image for the same model [Fig. 3(d1)]. Under the zone of stasis, a thick high-amplitude signal layer is seen, while the signal layer seen in the same depth region in the nonburn tissue is sparse and its amplitude is lower. The thick high-amplitude signal layer in the burn is attributable to potent dilatation of vessels in this region [Fig. 3(d2)]. Cloudy distribution of PA signals, which is thought to originate from vessels in the subcutaneous tissue, is commonly observed in the nonburn and burned tissue. However, the depth of the cloudy signal layer in the burn is slightly larger than that in the nonburn tissue, probably due to thickening of the skin because of collagen alteration and edema. Clinical burn diagnosis would not require such a 3-D image, but if needed, it can be easily obtained as demonstrated here.

3.3 Monitoring of the Burn Healing Process

Figure 5 shows PA images [Figs. 5(a1)–5(a3)] and the corresponding histological images with low and high magnifications [Figs. 5(b1)–5(b3)] of a DDB in the rats at one, three, and five days postburn. In the histological images, we observed unexpectedly early angiogenesis and it occurred at unexpectedly shallow depths in the dermis. In the histological images at day 1 [Fig. 5(b1)], there is a developing or juvenile blood vessel (yellow arrowheads). Correspondingly, we observed weak PA signals in the same depth region of the dermis in the PA image at one day postburn [white arrowhead in Fig. 5(a1)].
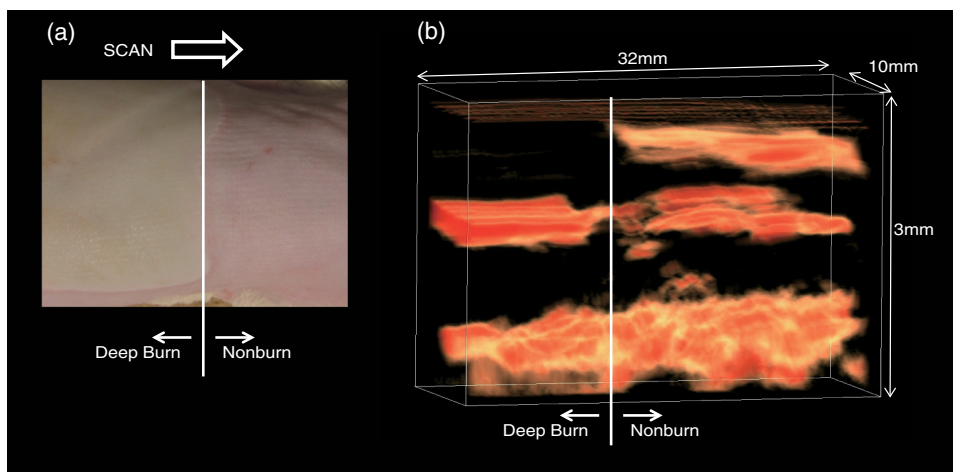

Fig. 4 Photograph (a) and three-dimensional PA image (b) of the DB-nonburn interface region in the rat dorsal skin.
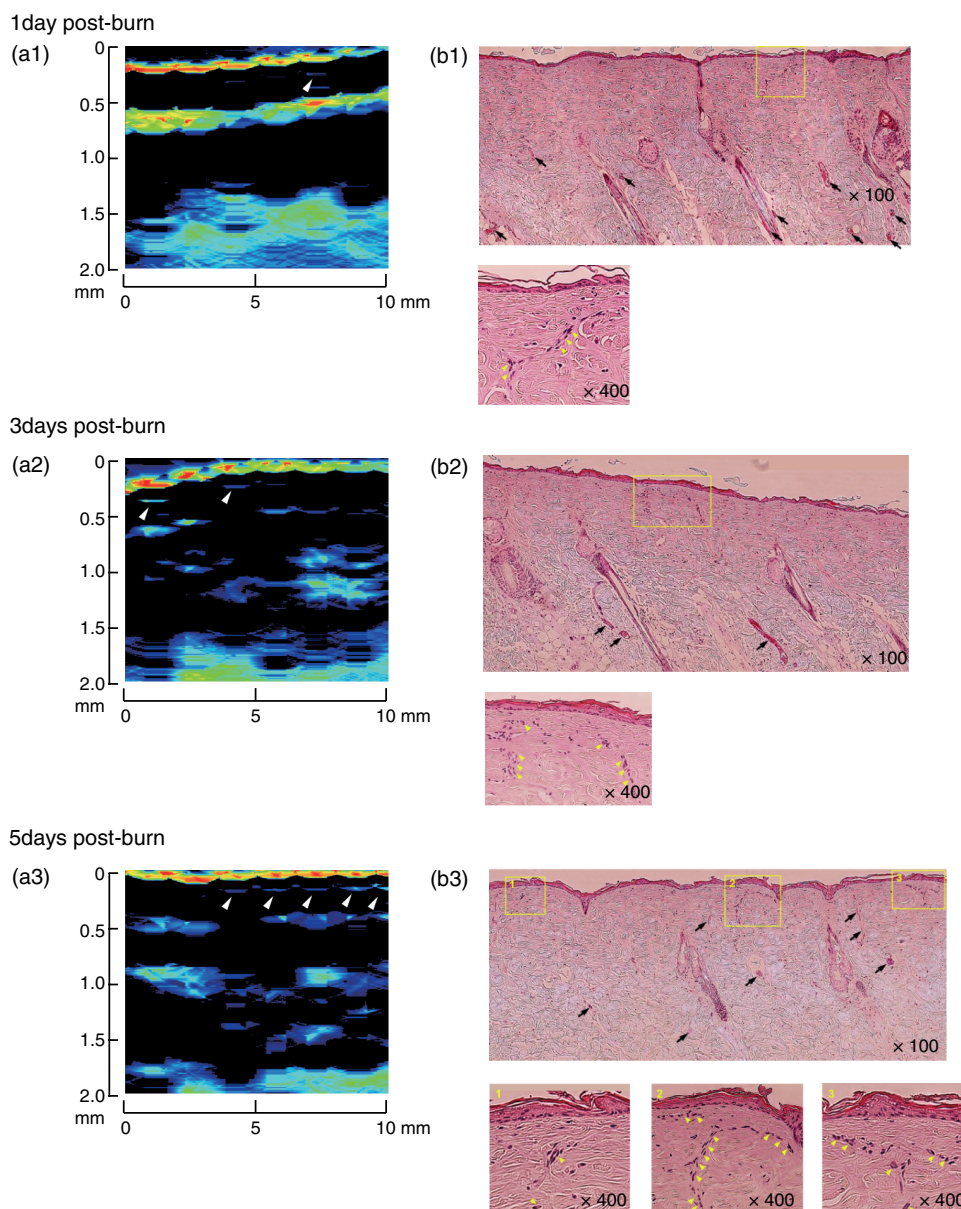
Fig. 5 PA images [(a1) to (a3)] and histological images with H&E staining [(b1) to (b3)] at one day, three days, and five days postburn. In (a1) to (a3), white arrowheads indicate PA signals that are thought to have originated from developing or juvenile blood vessels. In (b1) to (b3), magnified histological images (×400) of the regions indicated by yellow line rectangles are also shown. In the images with lower magnification (×100), black arrows indicate blood vessels; many of them are potently dilated at one and three days postburn. In the images with higher magnification, yellow arrowheads indicate developing or juvenile blood vessels.

The number of juvenile blood vessels increased with the elapse of time [Figs. 5(b2) and 5(b3)]. Correspondingly, the number of sites showing PA signals in the same depth regions increased [white arrowheads in Figs. 5(b2) and 5(b3)]; their amplitudes seem to have also increased, indicating a time-dependent increase in reperfusion due to wound healing. Change in the PA signals in the deep region of the dermis is also interesting. In the PA image at one day postburn [Fig. 5(a1)], a layer of strong signal is seen at a depth of ∼0.5 mm, which is attributable to many dilated blood vessels in the corresponding histological image [black arrows in Fig. 5(b1)]. There are still some potently dilated vessels at day 3 [Fig. 5(b2)], but dilation is reduced at day 5 [Fig. 5(b3)]. The amplitude of the corresponding PA

signals decreased with the elapse of time [Figs. 5(a2) and 5(a3)], also indicating a time-dependent wound healing process in burns. These findings suggest that the present PA imaging system is useful not only for assessing burn depths, but also for monitoring the wound healing process in burns.

4 Conclusion

In conclusion, we have developed a real-time PA imaging system for burn depth assessment. The phantom study showed the capability of imaging blood vessels in deep tissue (>4 mm). The in vivo study using rat burn models showed that differences in the depths of damaged tissue (zone of stasis) estimated by histological analysis and those indicated by PA imaging were

within 200 μm. The usefulness of the system for monitoring the burn healing process was also shown. On the basis of the results obtained in this study, we plan to conduct clinical studies on burn diagnosis in the near future.

References

1. S. A. Pape, C. A. Skouras, and P. O. Byrne, "An audit of the use of laser Doppler imaging (LDI) in assessment of burns of intermediate depth," *Burns* **27**, 233–239 (2001).
2. S. Jiao, W. Yu, and L. V. Wang, "Contrast mechanisms in polarization-sensitive Muller-matrix optical coherence tomography and application in burn imaging," *Appl. Opt.* **42**(25), 5191–5197 (2003).
3. N. Isono et al., "Early assessment of second degree burn depth by means of video microscope," *Jpn. J. Burn Inj.* **24**(1), 11–18 (1998).
4. S. Sato et al., "Photoacoustic diagnosis of burns in rats," *J. Trauma* **59**, 1450–1456 (2005).
5. H. F. Zhang et al., "Imaging acute thermal burns by photoacoustic microscopy," *J. Biomed. Opt.* **11**(5), 054033 (2006).
6. L. Vionnet et al., "24-MHz scanner for optoacoustic imaging of skin and burn," *IEEE Trans. Med. Imaging* **33**(2), 535–545 (2014).
7. S. Masuda, S. Niki, and M. Nakazawa, "Environmentally stable, simple passively mode-locked fiber ring laser using a four-port circulator," *Opt. Express* **17**(8), 6613–6622 (2009).
8. Y. Kawaguchi et al., "New polymer-based phantom for photoacoustic imaging," *Proc. SPIE* **8945**, 89450A (2014).
9. T. Vo-Dinh, *Biomedical Photonics Handbook*, CRC Press, Boca Raton (2003).
10. V. A. Shutilov, *Fundamental Physics of Ultrasound*, Gordon and Breach, New York (1988).
11. H. L. Walker and A. D. Mason Jr., "A standard animal burn," *J. Trauma* **8**(6), 1049–1051 (1968).
12. K. Aizawa et al., "Photoacoustic monitoring of burn healing process in rats," *J. Biomed. Opt.* **13**(6), 064020 (2008).

Biographies of the authors are not available.